Diamond & Related Materials 167 (2026) 113807

Contents lists available at ScienceDirect

Diamond & Related Materials

journal homepage: www.elsevier.com/locate/diamond

# Engineering diamond-based photocathodes for visible light-driven hydrogen generation

Alessandro Bellucci [a,*], Davide Barreca [b], Chiara Maccato [b,c], Ermanno Pierobon [c], Gian Andrea Rizzi [c], Gaetana Petrone [d,e], Andrea Liscio [d], Leonardo Mattiello [e], Eleonora Bolli [a], Matteo Mastellone [a], Raffaella Salerno [a,f], Riccardo Polini [f], Veronica Valentini [a], Daniele M. Trucchi [a]

[a] CNR-ISM, Sez. Montelibretti, DiaTHEMA Lab, 00015, Monterotondo (RM), Italy
[b] CNR-ICMATE and INSTM, Department of Chemical Sciences, Padova University, 35131, Padova, Italy
[c] Department of Chemical Sciences, Padova University and INSTM, 35131, Padova, Italy
[d] CNR-IMM, Sez. Roma, 00133, Roma, Italy
[e] Dipartimento di Scienze di Base e Applicate per l'Ingegneria, Sapienza Università di Roma, 00161, Roma, Italy
[f] Dipartimento di Scienze e Tecnologie Chimiche, Università di Roma "Tor Vergata", 00133, Roma, Italy

ARTICLE INFO

*Keywords:*
Ultra-nanocrystalline diamond
Nanotexturing
Nitrogen incorporation
Hydrogen plasma treatment
Water splitting

ABSTRACT

Diamond-based materials feature manifold attractive properties for different electrochemical applications, thanks to its chemical inertness and large operational bias window. Nevertheless, the blindness to Visible (Vis) light typically hinders their application in photo-electrochemistry using a sustainable source like solar radiation. In the present work, we propose an original all-carbon solution for the development of efficient photocathodes for hydrogen evolution with the functional integration of Vis light harvesting, charge transport, and interfacial processes in a single platform. The electrode is based on the implementation of surface nanostructuring by ultra-short pulsed laser on free-standing polycrystalline chemical vapor deposition (CVD) diamond plates. In particular, the photocathode is made up of micro-distributed graphitic paths in the inner material regions to reduce the series resistance and of a nitrogen-incorporated ultra-nanocrystalline layer as active element for the catalytic process. In photo-activated hydrogen evolution under Vis irradiation, the engineered cathode subjected to hydrogen plasma treatment yields a photocurrent of −0.14 mA/cm$^2$ at 0 V *vs.* the reversible hydrogen electrode (RHE) and a Tafel slope of −273 mV/dec. The present outcomes, related to the formation of defect-related surface states, open the door to the application of the proposed diamond-based structures in sustainable energy generation.

## 1. Introduction

The use of sunlight, a largely available natural resource, for the production of chemical fuels [1–4], has received an ever-growing attention to solve the global energy crisis and minimize the resulting ecological footprint. In this regard, photoelectrochemical water splitting has been extensively studied as a clean and sustainable route to convert solar energy into green hydrogen ($H_2$), a zero-emission and renewable energy vector [5]. Nonetheless, a widespread diffusion of this process inevitably requires a careful selection and engineering of active semiconductor photo-electrocatalysts, that are required to be stable, economically viable, and eco-friendly [6,7].

Diamond stands as an amenable candidate for various applications in electrochemistry thanks to its stability, its large operational bias window, and the widely variable electronic properties that can be customized as a function of processing conditions [8]. The first studies on diamond in such field date back to the 1990s, when boron-doped CVD diamond specimens yielded favorable performances as photo-electrochemical cathodes [9]. In comparison to the case of many other semiconductors, diamond surface modification introduces defect states which can play an active role in enhancing both light absorption and photogenerated charge carrier separation. In fact, one of the main advantages offered by diamond is the possibility of directly tuning its functional behavior through a controlled modulation of surface

* Corresponding author.
*E-mail address:* alessandro.bellucci@cnr.it (A. Bellucci).

https://doi.org/10.1016/j.diamond.2026.113807
Received 19 April 2026; Accepted 31 May 2026
Available online 1 June 2026

properties [10], for instance *via* termination with H-, O- or F-atoms [11]. In spite of these advantages, diamond is not generally regarded as an efficient water splitting electrocatalyst due to its large overpotentials for both hydrogen evolution reaction (HER) and oxygen evolution reaction [12]. Additionally, the wide diamond bandgap ($E_g > 5.0$ eV) requires UV light activation, accounting for a negligible part of the whole solar spectrum and precluding its efficient exploitation in the target process.

Nonetheless, the interest in diamond for similar applications is renewed in recent years [11,13,14] and various efforts have been devoted to engineering diamond electrodes, in order to render them Vis-light active and exploit solar light for their functional exploitation. In this context, different approaches have been proposed so far, among which the introduction of plasmonic nanoparticles [15,16], the controlled surface nanostructuring [17], and the fabrication of nanodiamond-based systems [18,19]. Nevertheless, whereas Vis-light absorption in diamond *via* $sp^2$-related states is well established to date [20–23], literature studies available to date do not properly address diamond-based systems in which absorption, charge transport, and catalysis are integrated in a single architecture. Yet, the latter solution would be more convenient in view of eventual practical end-uses.

In the present study, we propose an original and unprecedented engineering strategy enabling diamond to efficiently harvest Vis light for eventual water splitting applications. To this aim, we readapted and exploited a technology based on the diamond modification mainly with ultra-short laser pulses, earlier introduced for photon-enhanced electron emission converters [24]. The proposed structure (see Fig. 1) is made up of a nanotextured black diamond (BD) surface on a free-standing polycrystalline diamond plate, to efficiently absorb solar radiation [25,26]. Within the diamond plate, graphitic microelectrodes are written by femtosecond (fs)-laser processing. These conductive microcolumns serve as charge transport channels, lowering the series resistance [24,27] and facilitating charge carrier transfer between the BD layer and the active surface. Finally, the surface opposite to BD serves as support for an N-incorporated ultra-nanocrystalline (N-UNCD) active layer, which can be further functionalized *via* a controlled hydrogen plasma exposure. This structure, consisting entirely of diamond without additional constituents, allows to minimize interfacial losses and to enhance chemical stability.

The fabricated structures, *with* and *without* final hydrogen plasma exposure, have been subjected to a multi-technique characterization using a set of complementary advanced techniques, and finally tested as HER cathodes in water splitting processes under Vis light illumination. The performed analyses have enabled to attain a valuable insight into the interplay between material processing and the ultimate functional performances. Overall, the presently reported outcomes demonstrate an architecture-driven photoelectrochemical response in an all-carbon, diamond-based platform, in which hydrogen evolution is enabled through the functional integration of light harvesting, charge transport, and interfacial processes.

## 2. Materials and methods

### 2.1. Material synthesis and processing

Polycrystalline CVD free-standing diamond plates (Element Six, Diafilm™ Thermal Management grade, TM180) were selected as the starting material for photocathode fabrication. The samples consisted of $10 \times 10$ mm$^2$ plates with a thickness of 0.3 mm and a nominal in-plane thermal conductivity of ≈1800 W/m × K. These plates show a polished surface ($R_a < 50$ nm), and one lapped surface ($R_a < 250$ nm). Three distinct processing steps were carried out, each addressing one of the functional requirements to produce photocathodes for operations in aqueous electrochemical environments.

The first step aims at establishing conductive pathways across the plate thickness. In this regard, arrays of vertical graphitic microcolumns are inscribed within the 0.3 mm plate thickness using a femtosecond (fs) laser source (λ = 800 nm; duration = 100 fs duration; repetition rate = 1 kHz; amplified Ti:Sapphire system, Spectra-Physics, Milpitas, CA, USA; focusing geometry with a 40× objective, numerical aperture (NA) = 0.65, spot ≈10 μm). A pulse energy of 7 μJ and a scanning velocity of 64 μm/s were used, with the focal plane moving along the *z*-axis starting from the bottom to the upper surface forming continuous channels that enable the connection of two plate surfaces [24,27]. A square array of 2500 graphitic microelectrodes (50 × 50 columns, pitch Δ = 190 μm) is fabricated in the central sample region. After laser writing, the plates are immersed in acetone under ultrasonic agitation and rinsed with deionized water to remove residual debris.

In a second step, a light-absorbing surface is produced by irradiation

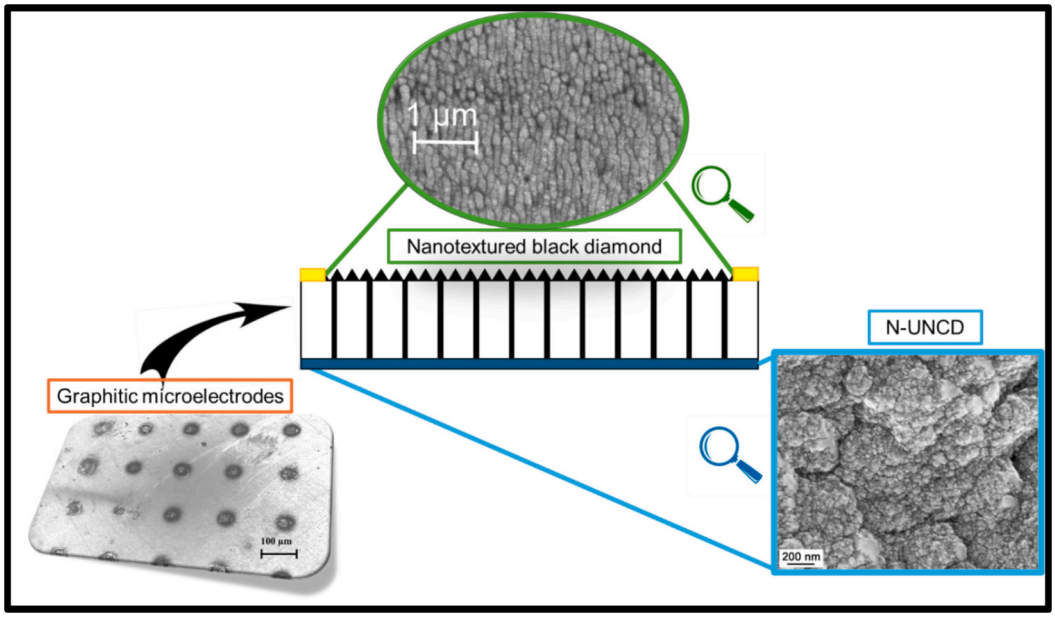


**Fig. 1.** Representative sketch of the proposed HER diamond photocathode based on black diamond (BD) surface, graphitic microelectrodes and N-UNCD layer (with or without hydrogen plasma exposure). Scanning electron microscopy (SEM) images for the three main components are shown [see also Fig. S2 in the Supporting Information (SI)].

in air of the TM180 plate polished face, using the same fs laser system. The beam is focused perpendicularly to the surface with a 4× objective (NA = 0.10), resulting in a spot diameter of (45 ± 3) μm, as determined *a posteriori* by the Liu method [28]. The diamond plate is raster-scanned under linearly polarized pulses. Scans are carried out with a 20 μm pitch between adjacent lines, a translation velocity of 1000 μm/s, and a pulse energy of 35 μJ. This treatment induces the formation of one-dimensional laser-induced periodic surface structures (LIPSS), yielding a black, optically absorbing layer with strongly enhanced visible light absorption compared to pristine diamond [29].

Finally, the lapped plate side is engineered *via* the deposition of a thin N-incorporated diamond layer by microwave plasma-enhanced CVD (MW-PECVD). The N-incorporated diamond layer is grown at 700 °C and 27 Torr, using a microwave power of 800 W. The feed gas mixture consisted of 200 standard cubic centimeters per minute (sccm) $H_2$, 2 sccm $CH_4$, and 15 sccm $N_2$. The deposition is carried out for 80 min, leading to a layer thickness of (140 ± 10) nm. This thickness represents the minimum value to produce a continuous film under the adopted operational conditions. In particular, an $N_2$ flux of 15 sccm was used, as preliminary studies performed in our CVD reactor identified this value as optimal for maximizing nitrogen incorporation. In fact, the latter starts saturating at ≈7% $N_2$, and a too high $N_2$ gas concentration (> 10%) induces a reduction of diamond growth-rate [30]. For one of the specimens (named as BD-N-UNCD-H hereafter), the surface is subsequently exposed to a hydrogen plasma (15 min at 700 °C, 800 W microwave power, and 27 Torr). Both samples were stored in air under ordinary laboratory conditions before characterization.

### 2.2. Characterization

Field emission-scanning electron microscopy (FE-SEM) micrographs were acquired with a Zeiss microscope (model Leo Supra 35; Oberkochen, Germany) using the InLens electron detector, at a primary beam accelerating voltage of 10 kV.

Atomic force microscopy (AFM) and Kelvin-probe force Microscopy (KPFM) analyses were performed using an OmegaScope platform (HORIBA Ltd., Kyoto, Japan) in tapping mode operational amplitude = 20 nm). A conductive Pt-coated pyramidal tip (MikroMasch HQ:NSC15/Pt; Wetzlar, Germany) with a characteristic radius of ≈30 nm, a resonance frequency of 325 kHz, and a work function of 4.5 ± 0.1 eV was used. The scan rate was maintained at 0.2 Hz. AFM and KPFM data were filtered, and analyzed using the AIST-NT SPM software. Work function evaluation was performed *via* a statistical data analysis, according to the methodology reported in Ref. [31].

X-ray photoelectron spectroscopy (XPS) and reflection electron energy loss spectroscopy (REELS) analyses were performed using a ThermoFisher ESCALAB QXi apparatus equipped with a monochromatized Al Kα X-ray source ($h\nu$ = 1486.6 eV), operating at a total pressure lower than $10^{-8}$ mbar. Survey spectra were collected in the binding energy (BE) range 0–1300 eV, using the following experimental settings: 100 eV analyzer pass energy; 1.0 eV/step; 0.05 s/step. High resolution core level (valence band) spectra were recorded using the following settings: analyzer pass energy of 50 eV (30 eV), corresponding to a resolution of 0.5 eV (0.3 eV); 0.02 eV/step; 0.05 s/step. Atomic percentages (at.%) were evaluated through peak area integration using ThermoFisher sensitivity factors. Peak fitting was carried out by the XPSPEAK software (version 4.1) [32] using a least-squares procedure, adopting a Shirley background and Gaussian-Lorentzian sum functions (typical mixing parameter = 0.2–0.3) [33]. REELS analysis was carried out using a primary electron beam energy of 1.0 keV. Energy gap values were obtained from the recorded spectra using the Avantage software provided by ThermoScientific (version 6.9.1, build 0004).

UV–Vis–NIR measurements were performed using a Cary 7000 system equipped with an integrating sphere in both total reflection (R) and transmission (T) geometries. For each sample, the absorptance (A%) was derived from the measurement of T% and R%, considering the relation A % = 100% – R% - T%, [26,29,34]. Illumination was directed from the side opposite to the BD, aiming to replicate the conditions of the photoelectrochemical tests.

### 2.3. Photoelectrochemical tests

Photoelectrochemical functional tests were performed at room temperature in $Na_2SO_4$ 0.1 M aqueous solution (pH = 6.5) with a standard three-electrode configuration, using an Autolab PGSTAT204 (Metrohm, Utrecht, The Netherlands) potentiostat/galvanostat. The used electrochemical cell [see Fig. S1 in the Supporting Information (SI)] was coupled to an optical bench (Metrohm Autolab) combined with the above instrument. Diamond-based materials were used as working electrodes, whereas a Pt wire and a saturated calomel electrode (SCE) were used as counter-electrode and reference electrode, respectively. The sample was contacted using a Cu adhesive strip attached to gold contacts pre-deposited on the diamond samples surface. Linear-sweep voltammetry (LSV) measurements were conducted using a scan rate of 5 mV/s, both in the dark and under illumination. In the latter case, the working electrode was irradiated from the front side (electrode-electrolyte interface) through a quartz window, using an incident light intensity of 100 mW/cm$^2$ (neutral white, Philips LUMILEDS) light emitting diode (LED) source. Applied bias photon-to-current efficiency (ABPE) (%) curves were obtained as: ABPE (%) = (|j × E| / P) × 100, [35] where j (mA/cm$^2$) is the photocurrent density at the potential E (V *vs.* RHE), and P is the incident light intensity.

## 3. Results and discussion

### 3.1. Characterization of the photocathode structures

In the present study, we develop all-carbon platforms functioning as Vis-light-activated photocathodes for water splitting processes. To this aim, a transparent CVD diamond plate was modified to fabricate a device capable of efficiently absorbing Vis photons, transporting photogenerated charges across its thickness, and activate redox reactions at the surface in contact with water. As reported in the Experimental section, the proposed structure is fabricated according to the following steps (Fig. 2a): 1) an array of conductive microelectrodes is formed within the commercial polycrystalline diamond; 2) a nanotextured BD layer is produced on one of the two surfaces; 3) a N-UNCD layer is deposited on the opposite surface; 4) the N-UNCD is eventually exposed to $H_2$-plasma treatment. Specifically, two photocathodes are investigated in this work, *without* and *with* the last step of hydrogen plasma exposure (named in the following as BD-N-UNCD and BD-N-UNCD-H, respectively). Fig. 2b shows the morphologies of the black diamond and the N-UNCD surfaces, respectively. The BD surface presents the typical morphology with the formed LIPSS [26], characterized by ripples with the expected periodicity of ≈170 nm and grooves extending up to several μm in length. On the other hand, the morphological features of the deposited layer, which follows the underlying substrate (see also Fig. S3 in the SI), are consistent with typical N-UNCD films grown by nitrogen-contained CVD conditions [36]. The root-mean-square (RMS) roughness of the N-UNCD layers [(78 ± 1) nm], lower than the pristine substrate [(97 ± 1) nm], indicated a certain degree of smoothing after the growth.

The surface chemical composition of the target systems, with particular regard to the presence of the various elements in different chemical environments as a function of the adopted processing conditions, is investigated by XPS. Upon going from BD-N-UNCD to BD-N-UNCD-H, wide-scan spectra (Fig. 3a) clearly show a net increase of oxygen content (from 1.3 at.% to 4.8 at.%; see also Fig. 3b), as well as the appearance of a weak, though well-detectable, nitrogen signal (0.8 at.%; see also Fig. 3c, as well as Table S1-S2 in the SI and the pertaining text for a detailed signal attribution). As a matter of fact, the higher O content presented by BD-N-UNCD-H should mainly be related to humid air

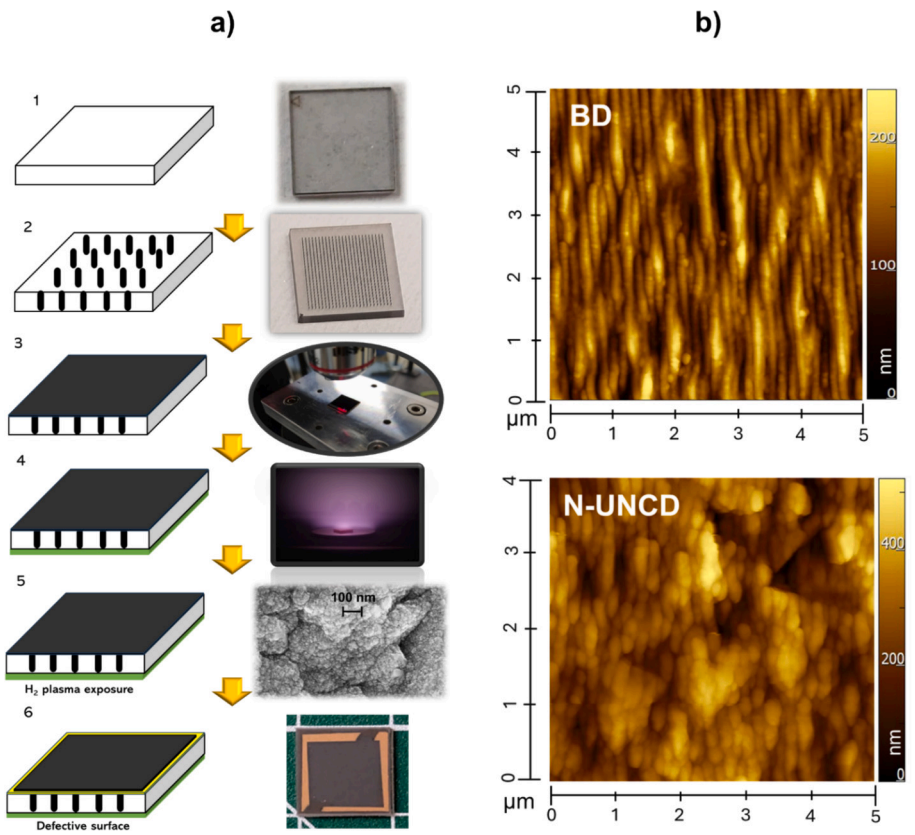


**Fig. 2.** a) Sketch of the adopted fabrication process: 1) commercial TM180 substrate as free-standing polycrystalline diamond plate; 2) graphitic microelectrodes within the plate connecting the two surfaces; 3) nanostructuring of the upper surface by fs-laser; 4) CVD of a N-incorporated layer on the bottom surface; 5) hydrogen plasma exposure of the previous layer (only for BD-N-UNCD-H); 6) metallic contact on the BD side. b) AFM image of BD and N-UNCD surfaces.

exposure prior to XPS analysis [37–39]. On the other hand, the $H_2$-plasma treatment promotes preferential etching of $sp^3$-bonded C, resulting in a relative increase of $sp^2$ carbon (see the $C_3$ component in Fig. 3d, right panel, and the discussion in the SI, pages S7–S8) [40]. On this basis, the appearance of N1s signal in BD-N-UNCD-H (Fig. 3c), at variance with BD-N-UNCD, can be likely related to the etching of near-surface regions induced by hydrogen plasma treatment, resulting in the detection of nitrogen previously buried below the surface [41]. In fact, nitrogen diffusion phenomena can be reasonably ruled out, being negligible at temperatures lower than 1500 °C [42].

For BD-N-UNCD-H, hydrogen can react with N-containing sites [43], yielding the formation of C-$NH_x$ (x = 1,2) groups (see the $N_2$ band in the N1s signal of Fig. 3c [44–46]). These moieties are also partially responsible for the $C_2$ contribution to the C1s signals [47–49] (Fig. 3d; see also the SI, pages S7-S8). The detected nitrogen signal can be reasonably attributed to surface-localized nitrogen functionalities associated with defect formation. Accordingly, XPS results indicate that the $H_2$-plasma treatment likely promotes a surface reconstruction of the N-UNCD layer, yielding a defect-rich surface generated by partial etching of the outermost carbon structure.

### 3.2. Functional tests

The HER activity of the two target systems was investigated by LSV measurements, both under illumination and in the dark (Fig. 4a-b). Whereas black diamond surfaces *with* and *without* $H_2$-plasma surface treatment did not present any significant photoactivity (Fig. S4 in the SI), due to a strong charge recombination at the surface as recently evidenced by advanced spectroscopic analyses [50], the situation turned out to be different for BD-N-UNCD systems, and the activity underwent a significant enhancement after hydrogen plasma exposure (compare Fig. 4a and b; see also Fig. 4c). The significantly enhanced efficiency of BD-N-UNCD-H in comparison to the homologous BD-N-UNCD specimen is also corroborated by a ABPE curves (see Fig. 4d). This enhancement can be traced back to the fact that $H_2$-plasma exposure induces the formation of a large amount of surface defects (see the above reported XPS results), yielding, in turn, improved functional performances.

It is worthwhile noticing that even the dark current density is significantly higher for BD-N-UNCD-H in comparison to BD-N-UNCD (dashed lines in Fig. 4a and b). This observation indicates that the presence of graphitic microcolumns alone is not sufficient to ensure an efficient charge carrier transport, since otherwise also BD-N-UNCD should show similar behavior in terms of electrical properties. Therefore, post-growth $H_2$-plasma treatment plays a crucial role in improving the overall material behavior by promoting the formation of surface states which, in turn, reduce the interfacial resistance and facilitate charge carrier collection at the electrode/electrolyte interface. This interpretation is consistent with the enhanced photocurrent gain observed under illumination. The analysis of the Tafel plots under illumination (Fig. 4f) highlights a more favorable HER kinetics for BD-N-UNCD-H, as indicated by the lower slope (−273 mV/dec) in comparison to BD-N-UNCD (−429 mV/dec), that did not undergo any $H_2$-plasma treatment.

To rationalize the present experimental observations, a sketch of a plausible mechanism governing material photoelectrochemical responses is proposed in Fig. 5a. The N-UNCD layer provides the electrochemically active interface with the electrolyte, where charge transfer to adsorbed species occurs. In this context, it is important to note that the high density of grain boundaries, defect states, and the presence of non-diamond carbon phases inherent to UNCD systems can significantly modify the interfacial charge-transfer properties. These features are therefore likely to contribute to the observed HER activity, in contrast to

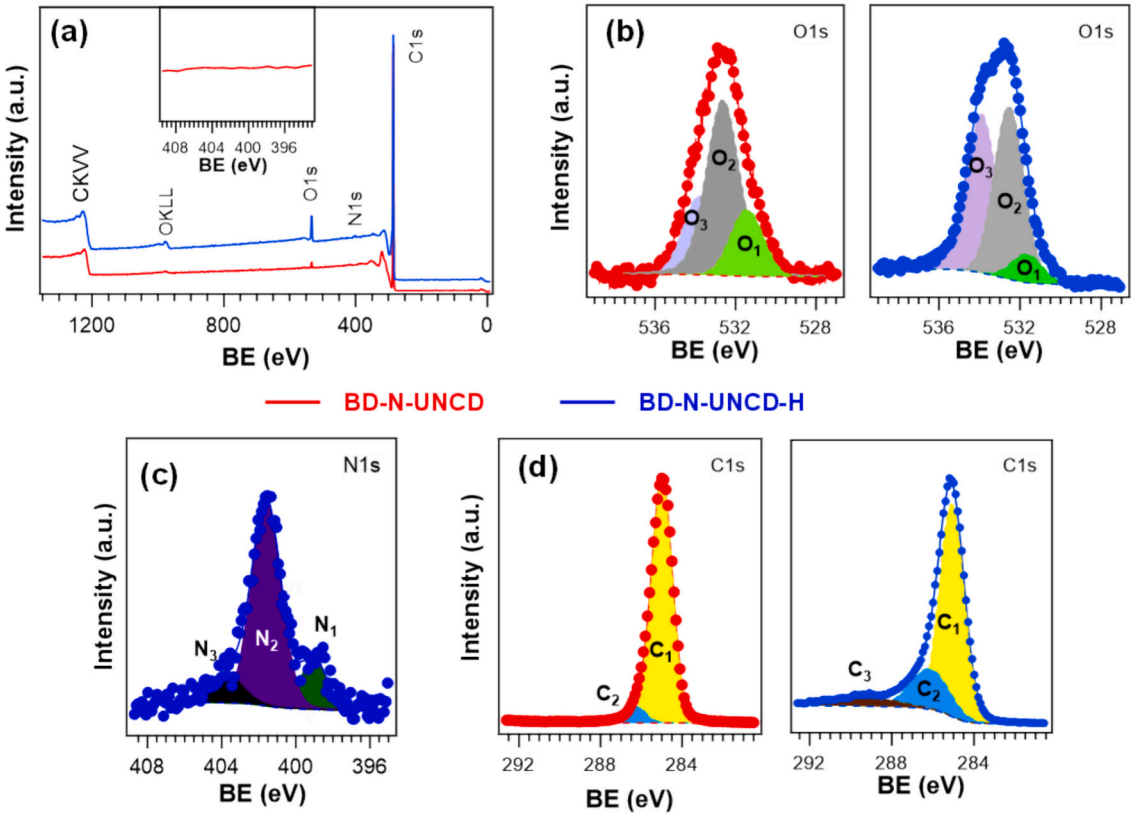


**Fig. 3.** a) XPS wide-scan spectra; b) O1s, c) N1s and d) C1s photoelectron peaks for BD-N-UNCD (red traces) and BD-N-UNCD-H (blue traces). For a detailed signal attribution, the reader is referred to Table S2 in the SI.

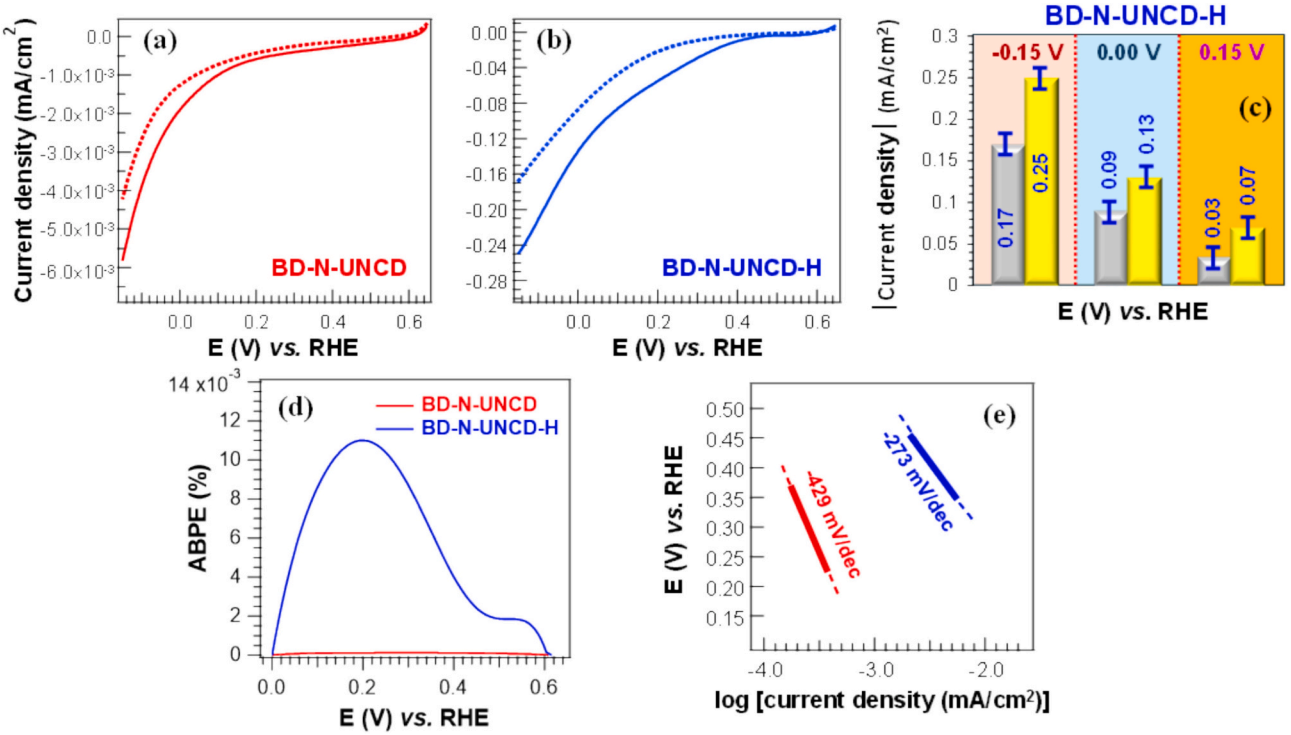


**Fig. 4.** Electrochemical characterization of the target systems as HER photocathodes. (a,b) LSV curves of current densities *vs.* applied potential. Dashed and continuous lines refer to dark and light conditions, respectively. (c) Current densities (grey: dark, yellow: light) at different bias values for sample BD-N-UNCD-H. (d) ABPE (%) curves. (e) Corresponding Tafel plots under illumination. Dashed and continuous lines correspond to experimental and fitting curves, respectively. The Tafel plots under dark conditions are displayed in Fig. S5 in the SI.

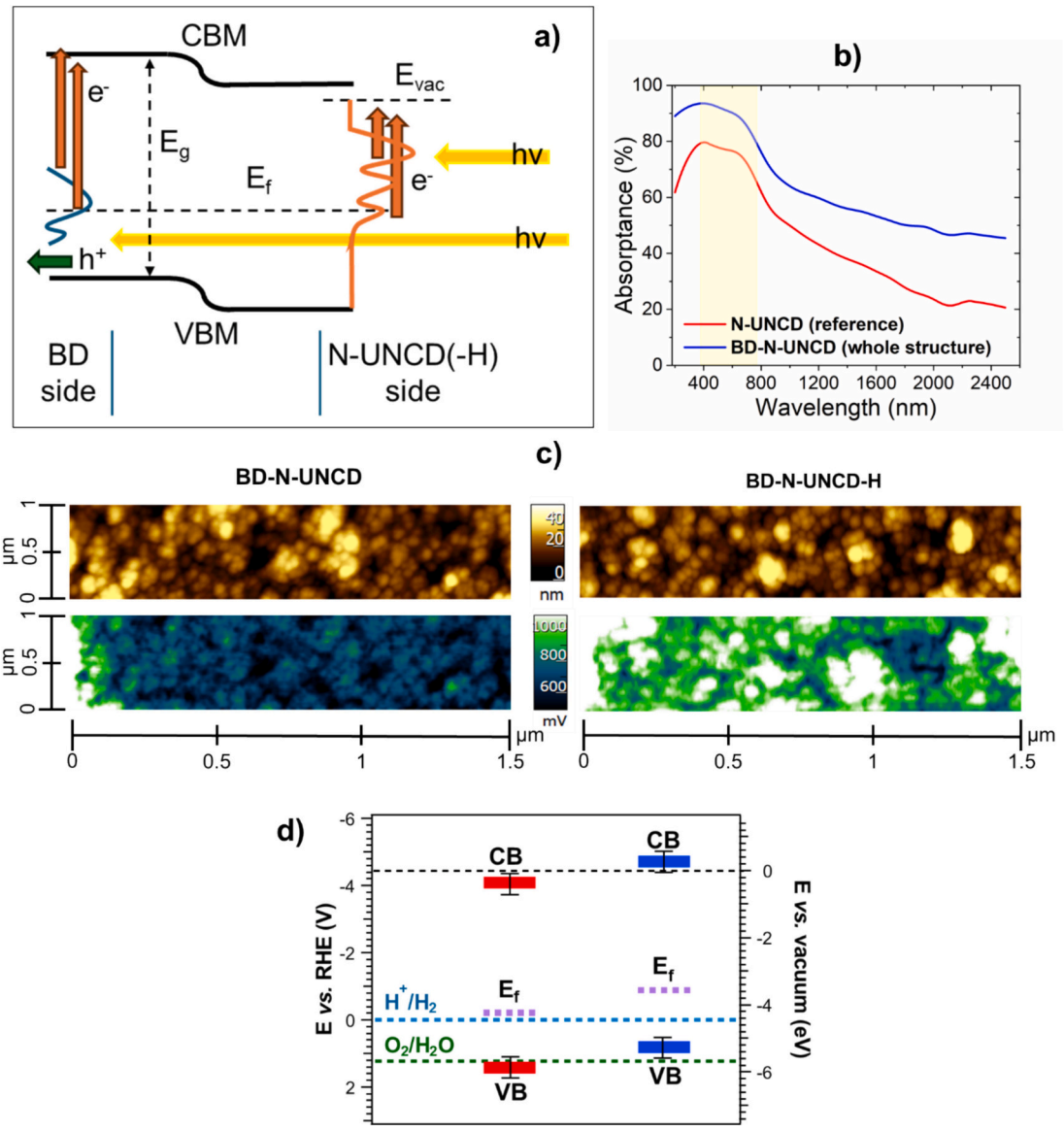


**Fig. 5.** a) Sketch of the mechanism for the HER performance for the BD-N-UNCD structures under illumination. VBM = valence band maximum; CBM: conduction band minimum; $E_f$ = Fermi level; $E_g$ = Energy gap; $E_{vac}$ = Vacuum level; b) Absorptance spectra for the BD-N-UNCD and a reference N-UNCD sample (without fs-laser treatments); c) AFM (top) and corresponding KPFM (bottom) maps for the work function evaluation; d) schematic energy band diagram of the target systems, obtained combining photoemission measurements and the work function values obtained by KPFM. VB = valence band edge; CB = conduction band edge; $E_f$ = Fermi level. The dashed lines from the top to the bottom mark the zero on the vacuum scale (vacuum level energy, $E_v$) and standard potentials of the $H_+/H_2$ and $O_2/H_2O$ redox couples, respectively. Electron affinity (EA) values are estimated as the difference between the conduction band edges (CB) and $E_v$.

the behavior typically reported for ideal, bulk diamond plates. However, due to its limited thickness and moderate conductivity, the N-UNCD layer cannot by itself sustain alone significant current densities without efficient charge replenishment from the substrate. Under dark conditions, graphitic microcolumns embedded within the plate reduce the overall series resistance, and provide preferential pathways for electron transport across the otherwise highly resistive matrix. The application of a post-growth $H_2$-plasma treatment further enhances the electrode response by modifying the N-UNCD layer electronic properties, thereby facilitating charge collection at the electrode/electrolyte interface. This effect explains the higher dark current observed for the $H_2$-plasma treated sample, and underscores the occurrence of improved carrier transport conditions. Under illumination, the mechanism likely involves the synergistic contribution of both the BD layer and the internal graphitic network. The BD surface exhibits enhanced sub-bandgap absorption associated with defect-related states and $sp^2$ contributions at the interface with the untreated region, which increases photocarrier generation within the diamond plate, even at locations distant from the active interface. These carriers can then be efficiently transported through graphitic microchannels toward the N-UNCD interface, where HER takes place, while the improved conductivity induced by $H_2$-plasma treatment enhances carrier extraction efficiency, yielding a higher overall photocurrent.

Based on the collected experimental results, the resulting photoresponse can hence be interpreted as an architecture-driven process in which light harvesting (BD layer), charge transport (graphitic microcolumns), and interfacial electrochemistry (N-UNCD surface) are spatially separated, but functionally integrated within the same diamond platform.

To attain a deeper insight into the interplay between material properties and photoelectrochemical response, UV–Vis–NIR optical analyses were performed (see Fig. 5b). The N-UNCD layer displays measurable sub-bandgap absorptance associated with its mixed $sp^3/sp^2$ character and defect-related states (Fig. 5b, red line). Upon integration

with the fs-laser-engineered BD region (Fig. 5b, blue line), a broadband absorption enhancement is observed throughout the entire spectral range. In particular, the increase is more pronounced in the NIR range (800–2000 nm), indicating that the fs-laser-engineered BD acts as a secondary absorber capable of harvesting photons with energy appreciably lower than the intrinsic diamond bandgap. As concerns the Vis range behavior, which is mainly of relevance in view of eventual practical end-uses, the BD–N-UNCD architecture exhibits an average absorptance increase of ≈20% relative to the reference configuration, consistent with the optical gain analysis reported in Fig. S6 (SI).

In an attempt to perform a qualitative evaluation of material light harvesting under the actual illumination conditions, a source-weighted absorption index was calculated using the emission spectrum of the LED employed during the photoelectrochemical testing (see SI, Fig. S7 and pages S11-S13). Since the illumination spectrum is identical for both specimens, the relative $I_{abs}$ variation yields information on the effective photon absorption of each system. The BD–N-UNCD structure shows an approximately 18% higher absorptance under LED illumination with respect to the reference configuration (N-UNCD). This value suggests that the optical gain is broadly distributed across the LED emission range, rather than being driven by isolated spectral regions. An overview of the relevant spectral intervals, their physical origin, and their expected impact on functional performances is provided in Table S3.

Overall, these findings demonstrate that laser-induced nanotexturing enhances radiation harvesting in the operative spectral range, supporting its role in increasing photocarrier generation. Based on these observations, the additional performance improvement observed after $H_2$-plasma treatment can be rationalized in terms of modifications of the surface electronic properties and enhanced interfacial charge-transfer processes, which are widely recognized as key factors governing electrocatalytic activity [51].

By combining work function measurements with photoemission data, a schematic energy band diagram (Fig. 5d) was derived. It should be noted that each technique probes different aspects of the electronic structure and brings intrinsic uncertainties; therefore, the present analysis has to be interpreted as indicative of relative changes in band alignment induced by surface treatment, rather than assigning quantitative electron affinity values. KPFM analysis (Fig. 5c, see also Table S4) estimates work function values of (3.9 ± 0.1) eV for the BD-N-UNCD sample and (3.5 ± 0.1) eV for BD-N-UNCD-H (its $H_2$-plasma treated counterpart). These values are in line with those reported in the literature for similar systems [52]. The Fermi level position relative to valence band maximum, estimated from XPS valence band spectra (Fig. S8 in the SI), was combined with bandgap measured by REELS (Fig. S9 in the SI). Taken together, these data suggest that $H_2$-plasma treatment, producing an etching of the outermost layers with the formation of defect states, induces a modification of electronic surface properties, leading to significant electrocatalytic performances.

Table S5 in the SI reports a comparison of the actual material HER performances with representative literature data for diamond-based cathodes. As can be observed, the performances of the specimen subjected to $H_2$-plasma treatment (BD-UNCD-H) are well positioned in the actual panorama, underscoring thus the potential of the adopted approach for possible additional implementations. In this regard, in view of eventual practical applications, the effect of material ageing was also assessed. In particular, the target electrodes were stored at room temperature under laboratory conditions for six months, and periodically subjected to electrochemical testing every 90 days. The obtained results (see Fig. S10 in the SI) enabled to exclude appreciable current density variations, underscoring thus a good stability of the target photocathodes. The outcomes of XPS analyses after six months of periodical electrochemical tests are reported in Fig. S11 in the SI. Deconvolution of the main core level peaks (Fig. S12 and Table S7 in the SI) evidenced, for both C1s signals, a contributing band centered at BE ≈ 289.2 eV ($C_3$), that could be attributed even to carboxylate/ester groups [44,53], consistent with the occurrence of a partial surface oxidation arising from exposure to the electrochemical environment and/or ambient air. In fact, quantitative analyses (Table S6 in the SI) indicated, for both samples, an oxygen content increase to a mean value of ≈ 13 at. %, and, in particular, of the overall weight of band $O_2$, in line with the above observations [53]. As concerns N1s signal, only band $N_2$, associated with $–NH_x$ groups, (see also Table S2 and related observations in the SI), was identified after electrochemical tests, likely due to surface chemical changes leading to the stabilization of amine-like N species.

Overall, the preliminary functional tests described so far highlight the applicative potential of the proposed structures. Since diamond is typically associated with relatively high overpotentials for HER [54], the observed system activity likely arises from the combined effects that drive the modulation of the interfacial processes. These factors can significantly modify interfacial charge transfer phenomena [55] and lead to measurable HER activity under conditions where pristine diamond would remain largely inactive.

## 4. Conclusions

Laser engineered-diamond photocathodes were successfully developed by introducing an original architecture in which light harvesting, charge transport, and interfacial reactivity are spatially separated, but functionally integrated. The most significant result is the coupling of an active electrolyte-surface interface (*i.e.,* the N-UNCD layer) with a template (*i.e.,* laser-engineered diamond plate) which has several advantages with respect to boron-doped diamond (in terms of visible-light absorption) or different substrates (like silicon), which can introduce internal barriers for the carriers' flow. After a detailed physico-chemical characterization by forefront complementary analytical tools, aimed at elucidating the interplay between the system characteristics and the adopted processing conditions, preliminary water splitting tests highlight a measurable HER performance under Vis light irradiation, that can be favourably amplified through a suitable processing of the active material. The observed behavior can be interpreted as an architecture-driven modulation of interfacial processes, rather than as an intrinsic diamond catalytic property.

Optical analyses demonstrate that the black diamond nanotexturing enhances photon harvesting within the operative visible window used for the performed testing. This consistency confirms that the optical gain is effectively distributed across the emission window of the light source and directly contributes to photocarrier generation under working conditions. In addition, $H_2$-plasma treatment of the N-UNCD layer yields a performance enhancement thanks to the generation of defect states, improving charge transport processes with respect to the *as-grown* N-UNCD layer.

Taken together, the results of the present work demonstrate that the adopted strategy stands as a promising tool to enhance the functional performances of a single all-carbon photocathode architecture. In fact, this study provides a benchmark for evaluating solar-to-chemical conversion efficiency and demonstrates the system's potential applicability under practical conditions. Based on the present data, additional perspectives for future research developments will concern an optimization of the system properties and performances for the target applications. To obtain a significant improvement of the performance and achieve competitive results with more conventional systems, an optimization of the charge transfer process at the catalytic surface could be obtained by finally tuning specific physical parameters, such as the N-UNCD film thickness, the level and uniformity of nitrogen incorporation, the crystallographic quality and thickness of the underlying polycrystalline diamond plate, and the depth and characteristics of the BD layer, as well as the effects of the $H_2$-plasma exposure with respect to the etching time. From a technological perspective, the fabrication strategy adopted in this work relies on processing techniques that are already compatible with industrial diamond manufacturing, such as fs-laser surface structuring and MW-PECVD. Further studies could include SIMS analyses to quantify impurity concentrations and assess compositional differences

between the samples. Additional electrical and spectroscopic investigations (Hall effect and transient absorption spectroscopy) may provide deeper insight into charge carrier properties and dynamics. Complementary experiments, including tests in deuterated water, could enable to shed further light into the process mechanism and extend the approach to other processes such as nitrogen and carbon dioxide reductions.

## CRediT authorship contribution statement

**Alessandro Bellucci:** Conceptualization, Data curation, Funding acquisition, Methodology, Supervision, Visualization, Writing – original draft, Writing – review & editing. **Davide Barreca:** Data curation, Formal analysis, Investigation, Methodology, Validation, Writing – review & editing. **Chiara Maccato:** Data curation, Formal analysis, Investigation, Validation, Writing – review & editing. **Ermanno Pierobon:** Data curation, Investigation, Methodology, Visualization. **Gian Andrea Rizzi:** Conceptualization, Data curation, Formal analysis, Investigation, Validation, Writing – review & editing. **Gaetana Petrone:** Data curation, Investigation, Visualization. **Andrea Liscio:** Data curation, Formal analysis, Methodology, Validation, Writing – review & editing. **Leonardo Mattiello:** Resources, Visualization. **Eleonora Bolli:** Data curation, Formal analysis, Investigation, Visualization. **Matteo Mastellone:** Investigation, Methodology, Software, Writing – review & editing. **Raffaella Salerno:** Investigation, Methodology, Visualization. **Riccardo Polini:** Formal analysis, Investigation, Methodology, Resources, Writing – review & editing. **Veronica Valentini:** Data curation, Investigation, Methodology. **Daniele M. Trucchi:** Formal analysis, Methodology, Supervision, Validation, Writing – review & editing.

## Declaration of competing interest

The authors declare that they have no known competing financial interests or personal relationships that could have appeared to influence the work reported in this paper.

## Acknowledgments

Funded by the European Union-Next Generation EU, Mission 4 Component 1, CUP B53D23015370006, MUR project SPEEDHY – "Solar PhotoElectrochEmical black Diamond converters for HYdrogen and ammonia production" (2022J9CEFM). The ThermoFisher ESCALAB QXi apparatus used in this work was funded by "*Sviluppo delle infrastrutture e programma biennale degli interventi del Consiglio Nazionale delle Ricerche (2019)*".

## Appendix A. Supplementary data

Supplementary data to this article can be found online at https://doi.org/10.1016/j.diamond.2026.113807.

## Data availability

Data will be made available on request.

## References

[1] J. Rongé, T. Bosserez, D. Martel, C. Nervi, L. Boarino, F. Taulelle, G. Decher, S. Bordiga, J.A. Martens, Monolithic cells for solar fuels, Chem. Soc. Rev. 43 (2014) 7963–7981.
[2] J.W. Ager, M.R. Shaner, K.A. Walczak, I.D. Sharp, S. Ardo, Experimental demonstrations of spontaneous, solar-driven photoelectrochemical water splitting, Energy Environ. Sci. 8 (2015) 2811–2824.
[3] N. Bora, A. Kumar Singh, P. Pal, U. Kumar Sahoo, D. Seth, D. Rathore, S. Bhadra, S. Sevda, V. Venkatramanan, S. Prasad, A. Singh, R. Kataki, P. Kumar Sarangi, Green ammonia production: process technologies and challenges, Fuel 369 (2024) 131808.
[4] S. Chu, W. Li, Y. Yan, T. Hamann, I. Shih, D. Wang, Z. Mi, Roadmap on solar water splitting: current status and future prospects, Nano Futures 1 (2017) 022001.
[5] H. Yoneyama, H. Sakamoto, H. Tamura, A photo-electrochemical cell with production of hydrogen and oxygen by a cell reaction, Electrochim. Acta 20 (1975) 341–345.
[6] S. Chen, L.-W. Wang, Thermodynamic oxidation and reduction potentials of photocatalytic semiconductors in aqueous solution, Chem. Mater. 24 (2012) 3659–3666.
[7] M.G. Walter, E.L. Warren, J.R. McKone, S.W. Boettcher, Q. Mi, E.A. Santori, N. S. Lewis, Solar water splitting cells, Chem. Rev. 110 (2010) 6446–6473.
[8] A. Fiorani, Y. Einaga, Fundamentals of diamond electrochemistry, ACS Electrochem. 1 (2025) 1983–2013.
[9] K. Patel, K. Hashimoto, A. Fujishima, Application of boron-doped CVD-diamond film to photoelectrode, Denki Kagaku Oyobi Kogyo Butsuri Kagaku 60 (1992) 659–661.
[10] S. Szunerits, C.E. Nebel, R.J. Hamers, Surface functionalization and biological applications of CVD diamond, MRS Bull. 39 (2014) 517–524.
[11] A. Chemin, L. Godeffroy, M. Rusu, M. Drisch, M. Finze, P. Knittel, A. Krueger, T. Petit, Modulating surface redox reactions and solvated Electron emission on boron-doped diamond by (photo)electrochemistry, PRX Energy 4 (2025) 033011.
[12] H.B. Martin, A. Argoitia, U. Landau, A.B. Anderson, J.C. Angus, Hydrogen and oxygen evolution on boron-doped diamond electrodes, J. Electrochem. Soc. 143 (1996) L133.
[13] R.J. Hamers, J.A. Bandy, D. Zhu, L. Zhang, Photoemission from diamond films and substrates into water: dynamics of solvated electrons and implications for diamond photoelectrochemistry, Faraday Discuss. 172 (2014) 397–411.
[14] D. Zhu, L. Zhang, R.E. Ruther, R.J. Hamers, Photo-illuminated diamond as a solid-state source of solvated electrons in water for nitrogen reduction, Nat. Mater. 12 (2013) 836–841.
[15] A. Bellucci, M. Mastellone, D. Catone, P. O'Keeffe, F. Martelli, G. Ammirati, A. Paladini, S. Turchini, F. Toschi, A. Santagata, M.L. Pace, R. Polini, R. Salerno, V. Valentini, D.M. Trucchi, Plasmonic silver nanoparticles facilitate Electron emission from diamond upon sun-like excitation, ChemPhotoChem 9 (2025) e202400202.
[16] S. Li, J.A. Bandy, R.J. Hamers, Enhanced photocatalytic activity of diamond thin films using embedded ag nanoparticles, ACS Appl. Mater. Interfaces 10 (2018) 5395–5403.
[17] P. Knittel, F. Buchner, E. Hadzifejzovic, C. Giese, P. Quellmalz, R. Seidel, T. Petit, B. Iliev, T.J.S. Schubert, C.E. Nebel, J.S. Foord, Nanostructured boron doped diamond electrodes with increased reactivity for solar-driven $CO_2$ reduction in room temperature ionic liquids, ChemCatChem 12 (2020) 5548–5557.
[18] T. Yoshikawa, H. Asakawa, T. Matsumoto, K. Ichikawa, A. Kaga, S. Yamamoto, R. Izumi, M. Ohno, T. Mahiko, M. Mutsuda, S. Yamasaki, N. Tokuda, CO2 reduction by visible-light-induced photoemission from heavily N-doped diamond nano-layer, Carbon 218 (2024) 118689.
[19] T. Yoshikawa, A. Kaga, K. Ichikawa, K. Hayashi, T. Matsumoto, R. Izumi, M. Ohno, S. Yamasaki, N. Tokuda, H. Asakawa, Enhanced performance of diamond electrodes with heavily N-doped surface nanolayers grown by CVD for high reduction current density, Electrochim. Acta 525 (2025) 146058.
[20] S. Bagheri, N. Muhd Julkapli, Nano-diamond based photocatalysis for solar hydrogen production, Int. J. Hydrog. Energy 45 (2020) 31538–31554.
[21] F. Buchner, T. Kirschbaum, A. Venerosy, H. Girard, J.-C. Arnault, B. Kiendl, A. Krueger, K. Larsson, A. Bande, T. Petit, C. Merschjann, Early dynamics of the emission of solvated electrons from nanodiamonds in water, Nanoscale 14 (2022) 17188–17195.
[22] B. Kiendl, A. Chemin, A.H. Day, R.B. Rodriguez, S. Choudhury, F. Buchner, K. Atak, C. Merschjann, E. Hadzifejzovic, T.D.W. Claridge, K. Larsson, A. Venerosy, M. M. Lounasvuori, N. Zabarska, B. Iliev, T.J.S. Schubert, H.A. Girard, J.-C. Arnault, J. S. Foord, T. Petit, A. Krueger, Intrabandgap states engineering in functionalized nanodiamond to generate solvated electrons for photocatalysis under solar illumination, Adv. Funct. Mater. 37 (2026) e23545, https://doi.org/10.1002/adfm.202523545.
[23] M. Khan, A. Hayat, S.K. Baburao Mane, T. Li, N. Shaishta, D. Alei, T.K. Zhao, A. Ullah, A. Zada, A. Rehman, W.U. Khan, Functionalized nano diamond composites for photocatalytic hydrogen evolution and effective pollutant degradation, Int. J. Hydrog. Energy 45 (2020) 29070–29081.
[24] M. Girolami, L. Criante, F. Di Fonzo, S. Lo Turco, A. Mezzetti, A. Notargiacomo, M. Pea, A. Bellucci, P. Calvani, V. Valentini, D.M. Trucchi, Graphite distributed electrodes for diamond-based photon-enhanced thermionic emission solar cells, Carbon 111 (2017) 48–53.
[25] A. Bellucci, P. Calvani, M. Girolami, S. Orlando, R. Polini, D.M. Trucchi, Optimization of black diamond films for solar energy conversion, Appl. Surf. Sci. 380 (2016) 8–11.
[26] P. Calvani, A. Bellucci, M. Girolami, S. Orlando, V. Valentini, R. Polini, D. M. Trucchi, Black diamond for solar energy conversion, Carbon 105 (2016) 401–407.
[27] M. Mastellone, A. Bellucci, M. Girolami, V. Serpente, R. Polini, S. Orlando, V. Valentini, A. Santagata, B. Paci, A. Generosi, M. Guaragno, D.M. Trucchi, Temperature-dependent electrical and structural characterization of laser-induced graphitic microwires in CVD diamond, Diam. Relat. Mater. 128 (2022).
[28] J.M. Liu, Simple technique for measurements of pulsed Gaussian-beam spot sizes, Opt. Lett. 7 (1982) 196–198.
[29] P. Calvani, A. Bellucci, M. Girolami, S. Orlando, V. Valentini, A. Lettino, D. M. Trucchi, Optical properties of femtosecond laser-treated diamond, Appl. Phys. A Mater. Sci. Process. 117 (2014) 25–29.

[30] S. Bhattacharyya, O. Auciello, J. Birrell, J.A. Carlisle, L.A. Curtiss, A.N. Goyette, D. M. Gruen, A.R. Krauss, J. Schlueter, A. Sumant, P. Zapol, Synthesis and characterization of highly-conducting nitrogen-doped ultrananocrystalline diamond films, Appl. Phys. Lett. 79 (2001) 1441–1443.
[31] R. Salerno, V. Valentini, E. Bolli, M. Mastellone, V. Serpente, A. Mezzi, L. Tortora, E. Colantoni, A. Bellucci, R. Polini, D.M. Trucchi, Low Electron affinity silicon/Nanocrystalline diamond Heterostructures for photon-enhanced thermionic emission, ACS Appl. Energy Mater. 7 (2024) 868–873.
[32] https://xpspeak.software.informer.com/4.1/.
[33] V. Jain, M.C. Biesinger, M.R. Linford, The Gaussian-Lorentzian sum, product, and convolution (Voigt) functions in the context of peak fitting X-ray photoelectron spectroscopy (XPS) narrow scans, Appl. Surf. Sci. 447 (2018) 548–553.
[34] P. Calvani, A. Bellucci, M. Girolami, S. Orlando, V. Valentini, R. Polini, D. M. Trucchi, Absorptance enhancement in fs-laser-treated CVD diamond, Phys. Status Solidi A 212 (2015) 2463–2467.
[35] M. Benedet, G.A. Rizzi, A. Gasparotto, L. Zeng, G. Pagot, E. Olsson, V. Di Noto, C. Maccato, D. Barreca, Efficient photoactivated hydrogen evolution promoted by $Cu_xO$–gCN–$TiO_2$–au (x = 1,2) nanoarchitectures, RSC Adv. 14 (2024) 7221–7228.
[36] R. Rouzbahani, K.J. Sankaran, P. Pobedinskas, K. Haenen, Advances in n-type chemical vapor deposition diamond growth: morphology and dopant control, Acc. Mater. Res. 5 (2024) 775–785.
[37] R. Akhvlediani, S. Michaelson, A. Hoffman, Interaction of water molecules with bare and deuterated polycrystalline diamond surface studied by high resolution electron energy loss and X-ray photoelectron spectroscopies, Surf. Sci. 604 (2010) 2129–2138.
[38] R. Flammini, M. Satta, A. Bellucci, M. Girolami, F. Wiame, D.M. Trucchi, Water desorption effects on the surface electrical resistance of air-exposed hydrogenated diamond, Appl. Surf. Sci. 512 (2020) 145491.
[39] S. Iacobucci, V. Serpente, D. Paoloni, D.M. Trucchi, F. Offi, A. Ruocco, Surface conductivity of air-exposed hydrogenated diamond: a survey into the subsurface electronic structure and the role of oxygen-related adsorbates, Appl. Surf. Sci. 693 (2025) 162688.
[40] H. Jiang, F. Liu, H. Yan, L. Si, Z. Dou, Etching effects of hydrogen plasma treatment on diamond surfaces, Surf. Coat. Technol. 363 (2019) 12–17.
[41] J. Birrell, J.A. Carlisle, O. Auciello, D.M. Gruen, J.M. Gibson, Morphology and electronic structure in nitrogen-doped ultrananocrystalline diamond, Appl. Phys. Lett. 81 (2002) 2235–2237.
[42] R. Jones, J.P. Goss, H. Pinto, D.W. Palmer, Diffusion of nitrogen in diamond and the formation of A-centres, Diam. Relat. Mater. 53 (2015) 35–39.
[43] M.N.R. Ashfold, J.P. Goss, B.L. Green, P.W. May, M.E. Newton, C.V. Peaker, Nitrogen in diamond, Chem. Rev. 120 (2020) 5745–5794.
[44] E. Scattolin, M. Benedet, D. Barreca, G.A. Rizzi, A. Gasparotto, C. Maccato, Graphitic carbon nitride functionalized with NiO nanoaggregates: an X-ray photoelectron spectroscopy investigation, Surf. Sci. Spectra 31 (2024) 024001.
[45] G. Marchiori, M. Brugia, T. Sturaro, M. Benedet, D. Barreca, A. Gasparotto, G. A. Rizzi, C. Maccato, ZnO and $ZnFe_2O_4$-functionalized graphitic carbon nitride: an XPS study, Surf. Sci. Spectra 32 (2025) 014003.
[46] M. Benedet, A. Gasparotto, G.A. Rizzi, D. Barreca, C. Maccato, G-$C_3N_4$-based materials functionalized with au, ag, and au-ag: an XPS study, Surf. Sci. Spectra 29 (2022) 024001.
[47] A. Chemin, M.K. Kuntumalla, M. Brzhezinskaya, T. Petit, A. Hoffman, Depth profiling of microwave nitrogen-terminated polycrystalline diamond surfaces by energy-dependent X-ray photoelectron spectroscopy, Appl. Surf. Sci. 661 (2024) 160082.
[48] R. Malkinson, M.K. Kuntumalla, A. Chemin, T. Petit, A. Hoffman, N. Bar-Gill, Enhanced quantum properties of shallow diamond atomic defects through nitrogen surface termination, J. Mater. Chem. C 12 (2024) 7206–7213.
[49] G. Marchiori, M. Benedet, A. Fasan, D. Barreca, C. Maccato, G.A. Rizzi, A. Gasparotto, XPS investigation of $Cu_xO$-functionalized amorphous carbon nitride, Surf. Sci. Spectra 31 (2024) 024010.
[50] A. Bellucci, A. Chemin, T. Petit, E. Bolli, V. Valentini, B.L. Cotts, A. Salleo, M. Girolami, S. Orlando, D.M. Trucchi, Origin of surface-induced visible light absorption of nanostructured diamond, MRS Bull. 51 (2026) 40–49.
[51] A. Chemin, L. Godeffroy, D. Amans, et al., The role of the Helmholtz potential on electrocatalytic activity, Nat. Commun. 17 (2026) 4547, https://doi.org/10.1038/s41467-026-70980-5.
[52] A. Chambers, D.J. McCloskey, N. Dontschuk, H.N. Al Hashem, B.J. Murdoch, A. Stacey, S. Prawer, A. Ahnood, Impact of surface treatments on the electron affinity of nitrogen-doped ultrananocrystalline diamond, Appl. Surf. Sci. 656 (2024) 159710.
[53] I. Bertóti, M. Mohai, K. László, Surface modification of graphene and graphite by nitrogen plasma: determination of chemical state alterations and assignments by quantitative X-ray photoelectron spectroscopy, Carbon 84 (2015) 185–196.
[54] J. Raymakers, K. Haenen, W. Maes, Diamond surface functionalization: from gemstone to photoelectrochemical applications, J. Mater. Chem. C 7 (2019) 10134–10165.
[55] A. Chemin, et al., Surface-mediated charge transfer of photogenerated carriers in diamond, Small Methods 7 (2023) 2300423.